Increasing Atmospheric Poleward Energy Transport with Global Warming

Yen-Ting Hwang,[1] Dargan M. W. Frierson,[1]

Most state-of-the-art global climate models (GCMs) project an increase in atmospheric poleward energy transport with global warming; however, the amount of increase varies significantly from model to model. Using an energy balance model that diffuses moist static energy, it is shown that: (1) the increase in atmospheric moisture content causes most of the increase in transport, and (2) changes in the radiation budget due to clouds explain most of the spread among GCMs. This work also shows that biases in clouds, surface albedo, ocean heat uptake, and aerosols will not only affect climate locally but will also influence other latitudes through energy transport.

1. Introduction

The atmospheric poleward energy transport, equal to the moist static energy (MSE) flux when kinetic energy transport is neglected, is one of the most fundamental aspects of the climate system. In midlatitudes, the atmospheric transport is much larger than the oceanic transport [Trenberth and Caron, 2001] and is partitioned approximately equally between dry static energy (DSE) flux and latent heat (LH) flux [Trenberth and Stepaniak, 2003]. The change in this quantity with global warming is important for predicting regional weather and climate, as energy transport connects climate phenomena across latitudes. For example, it impacts polar-amplified surface warming [Alexeev et al., 2005; Lu and Cai, 2010; Skific et al., 2009] and mediates shifts in the intertropical convergence zone [Kang et al., 2008].

From the dynamics point of view, eddy intensity and the efficiency with which eddies transport energy may vary with climate state [Green, 1970; Yin, 2005]. To predict changes in MSE flux, one has to consider both dry eddy dynamics and the amount of moisture eddies transport [Solomon, 2006; Frierson et al., 2007]. From the radiation point of view, the ultimate energy source of poleward energy transport is the meridional contrast in the distribution of net downward radiation at the top of the atmosphere (TOA) [Stone, 1978]. Changes in clouds, sea ice, and aerosols may introduce variations in radiative fluxes at the TOA, and thus have potential to change the MSE flux.

In this study, we analyze the change in MSE flux with global warming using global climate model (GCM) data from the Coupled Model Intercomparison Project Phase 3 (CMIP3) of the World Climate Research Program database. Held and Soden [2006] (see also the corrigendum of Hwang et al. [2010]) analyzed the multi-model mean of this change, while we examine both the multi-model mean and the inter-model spread. The differences among models provide a unique opportunity to understand factors that influence the energy transport.

[1]Department of Atmospheric Sciences, University of Washington, Seattle, Washington USA.

2. Results from GCMs and interpretation with an energy balance model (EBM)

As listed in Table 1, we study the response to global warming in equilibrium simulations of slab ocean models and in two sets of transient coupled GCM simulations, the climate of the 20th century experiment (20C3M) and the SRES A1B scenario. The MSE fluxes (F_M) in the simulations are calculated by integrating the energy budget in the atmosphere, i.e., the differences between net (downward) energy fluxes at the TOA (R_T) and at the surface (F_s)

$$R_T = \bigtriangledown \cdot F_M + F_s \qquad (1)$$

$$F_M(\phi) = \int_{-\frac{\pi}{2}}^{\phi} \int_0^{2\pi} (R_T - F_s) \ a^2 cos\phi d\lambda d\phi, \qquad (2)$$

where a is the radius of the earth, ϕ is latitude, and λ is longitude. To evaluate the change in MSE flux, we calculate the difference between the warmer and the control periods listed in Table 1.

The change in northward MSE flux in each model is plotted in Fig. 1. Most models show increasing poleward transport in both hemispheres in all of the simulations, although the magnitude of the increase varies significantly. For instance, in the A1B scenario at 40S, one model projects nearly twice the ensemble mean change, while others project less than one-third of the ensemble mean change. Similar ranges are found for the other scenarios and other latitudes.

The increase in MSE flux in the GCMs is associated with an increase in LH flux and a compensating but smaller decrease in DSE flux (Fig. 2 of Hwang et al. [2010]). We next demonstrate that this increase can be understood with a one-dimensional energy balance model (EBM) [Sellers, 1969; Budyko, 1969] with constant MSE diffusivity.

A detailed description of the EBM is in the Appendix. In short, the EBM predicts the two terms that are strong functions of temperature, outgoing longwave radiation (OLR) in clear sky and surface MSE, given the zonal average net incoming shortwave (SW) radiation at the TOA, longwave (LW) cloud radiative forcing (CRF), and vertical fluxes at the surface. The diffusive nature of the EBM implies that in response to a localized heating at a particular latitude, there is both local increase in OLR and increased diffusive transport away, with the partition between the two determined by the diffusivity constant. We find that using the same diffusivity across all latitudes, in all of the models, and in both the control and the warmer climate is sufficient to understand the changes in MSE flux in GCMs.

The result of the EBM at 40 degrees N and S is shown in Fig. 2. The EBM predicts the correct sign of the changes in MSE fluxes in all of the GCMs, and is additionally able to explain much of the spread among individual GCMs in all three scenarios. The EBM overpredicts the fluxes slightly in the SH, while there is a small underprediction in the NH.

While traditional EBMs simply diffuse temperature, we diffuse MSE which is conserved even in the presence of LH release [Frierson et al., 2007]. Including moisture is essential to capturing the increase of poleward MSE flux. The

increasing water vapor content in the warmer climate leads to increasing LH flux, which is the primary cause of the systematic increase of the MSE flux in midlatitudes. The EBM accomplishes this even in response to a uniform warming by increasing water vapor preferentially in low latitudes (due to nonlinearity of Clausius-Clapeyron relation). Dry EBMs cannot capture such an increase without increasing diffusivity in the warmer climate (not shown).

3. Analyzing attributions of increasing MSE flux and inter-model spread

We next examine term-by-term how components of the energy budget bring about changes in energy transport. We use the approximate partial radiative perturbation (APRP) method [Taylor et al., 2007] to separate the GCM changes in net incoming shortwave radiation (S) into three terms: surface albedo (I), cloud SW (C_S), and noncloud SW (A_S) effects. Together with changes in greenhouse gases (G), longwave cloud radiative forcing (C_L) and surface flux (O), these comprise the 6 additional terms we prescribe in the EBM when predicting MSE flux in the warmer period. Fig. 3 illustrates the latitudinal dependence of these six terms, including the multi-model mean (solid line) and the inter-model spread (shading).

We prescribe these six terms one term at a time to perform an attribution study on the changes in energy transport for each model. The sum of the six single term EBM changes is nearly identical to the EBM-predicted change that considers all of the six terms at once (x-axis in Fig. 2) in all cases. Fig. 4 demonstrates how the individual terms in Fig. 3 affect the ensemble mean MSE flux in the EBM at 40N/S, and the second-most extremes of each term are labeled with error bars to represent the spread of models.

3.1. Greenhouse gases (G)

We assume the greenhouse effect is uniform across latitudes and its strength is the same in all models in the control climate. The greenhouse effect in the warmer climate is tuned to fit the magnitude of each GCM's global mean temperature change (see Appendix for details). The prescribed changes of greenhouse effect are uniform across latitudes (G in Fig. 3), but the moisture preferentially increases in low latitudes leading to an increase in equator-to-pole MSE gradient, and thus an increase in MSE flux. This is the dominant contribution to the increase in fluxes in both transient scenarios (G in Fig. 4), which explains why traditional temperature-diffusing EBMs fail to capture the increasing fluxes. This term contributes a rather small amount to the model-to-model differences however.

3.2. Surface albedo (I)

In a warmer climate, melting snow and ice reduces albedo especially at high latitudes (I in Fig. 3), which increases temperature in high latitudes, flattens the MSE gradient and results in a decrease in the poleward MSE flux in the EBM (I in Fig. 4). The slab simulations have a significantly larger surface albedo effect in the SH compared with the A1B simulations, while there are similar amounts of melting in the NH in these two scenarios. Surface albedo contributes a significant amount to the models' spread at 40N in the A1B scenario.

3.3. Cloud SW (C_S)

There are two main structures of cloud changes that affect SW fluxes at the TOA (C_S in Fig. 3): low cloud coverage tends to decrease in lower latitudes, and cloud cover tends to increase in regions of decreasing sea ice [Trenberth and Fasullo, 2009]. Increasing clouds in high latitudes partially offsets the surface albedo change and cools the region. Both of these cloud structures lead to an increase in poleward MSE flux (C_S in Fig. 4). SW cloud effects are the dominant reasons the MSE fluxes increase in the slab simulations, and are second in importance in the two other scenarios. Differences in this term among models lead to the largest differences in predicted fluxes in all three scenarios, surpassing all other terms, especially in the SH.

3.4. Cloud LW (C_L)

We use changes in LW CRF to estimate the changes of TOA LW fluxes caused by variation in clouds [Cess et al., 1990]. We use this method rather than more accurate methods to calculate cloud contribution to changing TOA LW fluxes (e.g., Wetherald and Manabe [1988] and Soden et al. [2008]) to be consistent with the L_C we prescribe in the control period. In high latitudes, increasing high cloud coverage causes a warming of those regions while in the subtropics, LW cloud effects cause a cooling (C_L in Fig. 3). LW cloud effects thus lead to a decrease in midlatitude energy fluxes in both hemispheres in all scenarios (C_L in Fig. 4). Cloud LW effects are also associated with much of the model-to-model variance in midlatitude fluxes.

3.5. Surface Flux (O)

The surface flux term includes contributions from both changes in ocean circulation and differential ocean heat uptake. This term should be near zero in the slab simulations which do not allow changes in ocean heat transport, but most models show negative tendencies around the sea ice melting area. In the transient simulations, the primary features of this field are a negative anomaly in the high latitudes of the SH, and a smaller negative anomaly in the high latitude NH (O in Figure 3). This burying of heat in high latitudes allows MSE fluxes to remain large in the midlatitudes, and this term contributes significantly to both the ensemble mean fluxes and the models spread (O in Figure 4).

3.6. Noncloud SW (A_S)

The noncloud SW term calculated by the APRP method describes the changes TOA SW fluxes that are not associated with clouds nor surface albedo. This includes absorption changes from increasing water vapor and CO_2, which provide an approximately globally uniform background positive value, and the effect of changes in scattering and absorption by aerosols, which tend to be localized in the Northern midlatitudes in the two transient scenarios (A_S in Fig. 3). This term causes a small increase in flux in the EBM at 40N/S in the slab and A1B simulations and the models spreads are small.

4. Concluding Remarks

This paper demonstrates how the changes in vertical energy fluxes at the TOA and at the surface influence horizontal MSE flux in midlatitudes, thus causing these changes to be felt non-locally. The EBM facilitates attribution of changes in MSE fluxes to individual climate components. The uniform warming caused by greenhouse gases, and the concurrent increase in moisture content is the primary reason that the MSE flux increases in warmer climates. The

change in cloud SW effect is the dominant source of uncertainty among models.

The EBM with a fixed MSE diffusivity explains the spread in increasing poleward atmospheric energy transport. Variations in atmospheric dynamics in the different models are not needed to understand the differences among models, and there is no compelling evidence for a change in atmospheric diffusivity with warming. It is important to note, however, that many of the climate components which we prescribe in the EBM are likely influenced by changes in circulation. For instance, some of the changes in clouds in the simulations appear to be related to the shifting of storm tracks.

This study suggests that constraining uncertainties in the climate components such as clouds and surface albedo will not only narrow down the range of GCM projected global mean temperature change, but will also benefit regional climate predictions through a more confident projection of atmospheric energy transport.

Appendix: Energy Balance Model

MSE Flux in the Control Period

Starting with the atmospheric energy budget (1), we assume the MSE flux at a given latitude is proportional to the surface MSE gradient

$$S - (L_S - L_C) = -\frac{p_s}{g} D \, \bigtriangledown^2 m + F_s, \qquad (3)$$

where S is the net solar radiation at TOA, L_S is the OLR in clear sky, L_C is the LW CRF (OLR in clear sky minus OLR in all sky), p_s is the surface pressure $9.8 \times 10^4 \ Pa$, D is the diffusion coefficient, $m = c_p T + Lq$ is the MSE at the surface, and F_s is the downward surface flux. In the EBM, we prescribe the zonal average of three terms from the GCM data: S, L_C, and F_s. The other two terms, L_S and $-\frac{p_s}{g} D \bigtriangledown^2 m$, are both made functions of surface temperature, T_s. The surface moist static energy is calculated assuming a flat surface and 80% relative humidity. L_S is linearized to be $aT_s - b$, with $a = 2.07$ and $b = 332.4$ in the control period, calculated from a linear regression of the 20C3M data. The latitudinally uniform diffusion coefficient $D = 1.06 \times 10^6 \ m^2/s$ is tuned to best fit the zonal mean T_s profile from 1980 to 1999 in the 20C3M simulations.

MSE Flux in the Warmer Period

The warmer period energy budget equation is

$$(S+I+C_S+A_s)-(L_S'-(L_C+C_L)) = -\frac{p_s}{g}D\bigtriangledown^2 m'+(F_s-O), \qquad (4)$$

where I, C_S, and A_s are the increases in incoming SW at the TOA due to changes in surface albedo, clouds, and other components, respectively. L_S' is the warmer period OLR in clear sky, C_L is the increase in LW CRF, m' is the warmer period surface MSE, and O is the increase in upward surface flux. The terms I, C_s, and A_s are calculated with the APRP method. C_L and O are derived from GCMs outputs. We modify the constant b' in $L_S' = aT_s' - b'$ to fit the climate sensitivity of each GCM and to simulate the enhanced greenhouse effect. We use the same D for the warmer period. The predicted quantities in the EBM are m', T_s', L_s', and the MSE flux.

The Change of MSE Flux

The predicted change of MSE flux is the difference between the predicted MSE flux in the warmer period and in the control period. It can be written as Eqn.(4) - Eqn.(3):

$$F_M'(\phi)-F_M(\phi) = \int_{-\frac{\pi}{2}}^{\phi} \int_0^{2\pi} \left[-\frac{p_s}{g}D\bigtriangledown^2(m'-m)\right] a^2 cos\phi d\lambda d\phi$$

$$= \int_{-\frac{\pi}{2}}^{\phi} \int_0^{2\pi} \left[-(L_S'-L_S)+S+I+C_S+C_L+O\right] a^2 cos\phi d\lambda d\phi, \qquad (5)$$

where the latitudinal distributions of m', m, L_S', and L_S are calculated by the EBM. S, I, C_S, C_L, and O can influence both m' and L_S'.

References

Alexeev, V., P. Langen, and J. Bates, 2005: Polar amplification of surface warming on an aquaplanet in ghost forcing experiments without sea ice feedbacks. *Climate Dynamics*, **24 (7)**, 655–666.

Budyko, M. I., 1969: The effect of solar radiation variations on the climate of the earth. *Tellus*, **21 (5)**, 611–619.

Cess, R. D., et al., 1990: Intercomparison and interpretation of climate feedback processes in 19 atmospheric general circulation models. *J. Geophys. Res.*, **95**.

Frierson, D. M. W., I. M. Held, and P. Zurita-Gotor, 2007: A gray-radiation aquaplanet moist GCM. part II: Energy transports in altered climates. *Journal of the Atmospheric Sciences*, **64 (5)**, 1680–1693.

Green, J. S. A., 1970: Transfer properties of the large-scale eddies and the general circulation of the atmosphere. *Quarterly Journal of the Royal Meteorological Society*, **96 (408)**, 157–185.

Held, I. M. and B. J. Soden, 2006: Robust responses of the hydrological cycle to global warming. *Journal of Climate*, **19 (21)**, 5686–5699.

Hwang, Y.-T., D. M. W. Frierson, B. J. Soden, and I. M. Held, 2010: The corrigendum for Held and Soden (2006). *Journal of Climate*, in press.

Kang, S. M., I. M. Held, D. M. W. Frierson, and M. Zhao, 2008: The response of the ITCZ to extratropical thermal forcing: Idealized slab-ocean experiments with a GCM. *Journal of Climate*, **21 (14)**, 3521–3532.

Lu, J. and M. Cai, 2010: Quantifying contributions to polar warming amplification in an idealized coupled general circulation model. *Climate Dynamics*, **34 (5)**, 669–687.

Sellers, W. D., 1969: A global climatic model based on energy balance of the earth-atmosphere system . Journal of Applied Meteorology, 392-400 pp.

Skific, N., J. A. Francis, and J. J. Cassano, 2009: Attribution of projected changes in atmospheric moisture transport in the arctic: A self-organizing map perspective. *Journal of Climate*, **22 (15)**, 4135–4153.

Soden, B. J., I. M. Held, R. Colman, K. M. Shell, J. T. Kiehl, and C. A. Shields, 2008: Quantifying climate feedbacks using radiative kernels. *Journal of Climate*, **21 (14)**, 3504–3520.

Solomon, A., 2006: Impact of latent heat release on polar climate. *Geophys. Res. Lett.*, **33 (7)**, L07 716.

Stone, P. H., 1978: Constraints on dynamical transports of energy on a spherical planet. *Dynamics of Atmospheres and Oceans*, **2 (2)**, 123–139.

Taylor, K. E., M. Crucifix, P. Braconnot, C. D. Hewitt, C. Doutriaux, A. J. Broccoli, J. F. B. Mitchell, and M. J. Webb, 2007: Estimating shortwave radiative forcing and response in climate models. *Journal of Climate*, **20 (11)**, 2530–2543.

Trenberth, K. E. and J. M. Caron, 2001: Estimates of meridional atmosphere and ocean heat transports. *Journal of Climate*, **14 (16)**, 3433–3443.

Trenberth, K. E. and J. T. Fasullo, 2009: Global warming due to increasing absorbed solar radiation. *Geophys. Res. Lett.*, **36 (7)**, L07 706.

Trenberth, K. E. and D. P. Stepaniak, 2003: Covariability of components of poleward atmospheric energy transports on seasonal and interannual timescales. *Journal of Climate*, **16 (22)**, 3691–3705.

Wetherald, R. and S. Manabe, 1988: Cloud feedback processes in a general circulation model. *Journal of the Atmospheric Sciences*, **45 (8)**, 1397–1416.

Yin, J. H., 2005: A consistent poleward shift of the storm tracks in simulations of 21st century climate. *Geophys. Res. Lett.*, **32 (18)**, L18 701.

Table 1. Simulations and models

	Control Period	Warmer Period	Models Used*
slab	the mean of last 20 yr in slab control equilibrium run	the mean of last 20 yr in 2xCO2 equilibrium run	CCCMA CGCM3 (T63), CCCMA CGCM3 (T47), GFDL CM2.0, INM CM3, MIROC (hires), MIROC (medres), MPI ECHAM5, MRI CGCM2, UKMO Hadgem1
A1B Scenario	the mean of 2001 to 2020	the mean of 2081 to 2100	CCCMA CGCM3 (T47), GFDL CM2.0, GFDL CM2.1, IAP FGOALS1, INM CM3, MIROC (hires), MIROC (medres), MIUB ECHO, MPI ECHAM5, MRI CGCM2, NCAR CCSM3, UKMO Hadgem1, UKMO HadCM3
20C3M	the mean of 1901 to 1920	the mean of 1980 to 1999	CCCMA CGCM3 (T63), CCCMA CGCM3 (T47), CNRM CM3, GFDL CM2.0, IAP FGOALS1, INM CM3, IPSL CM4, MIROC (hires), MIROC (medres), MIUB ECHO, MPI ECHAM5, MRI CGCM2, NCAR CCSM3, UKMO Hadgem1, UKMO HadCM3

*Some models in the CMIP3 archive are omitted due to missing variables. Only run 1 of each simulation is used in the analysis.
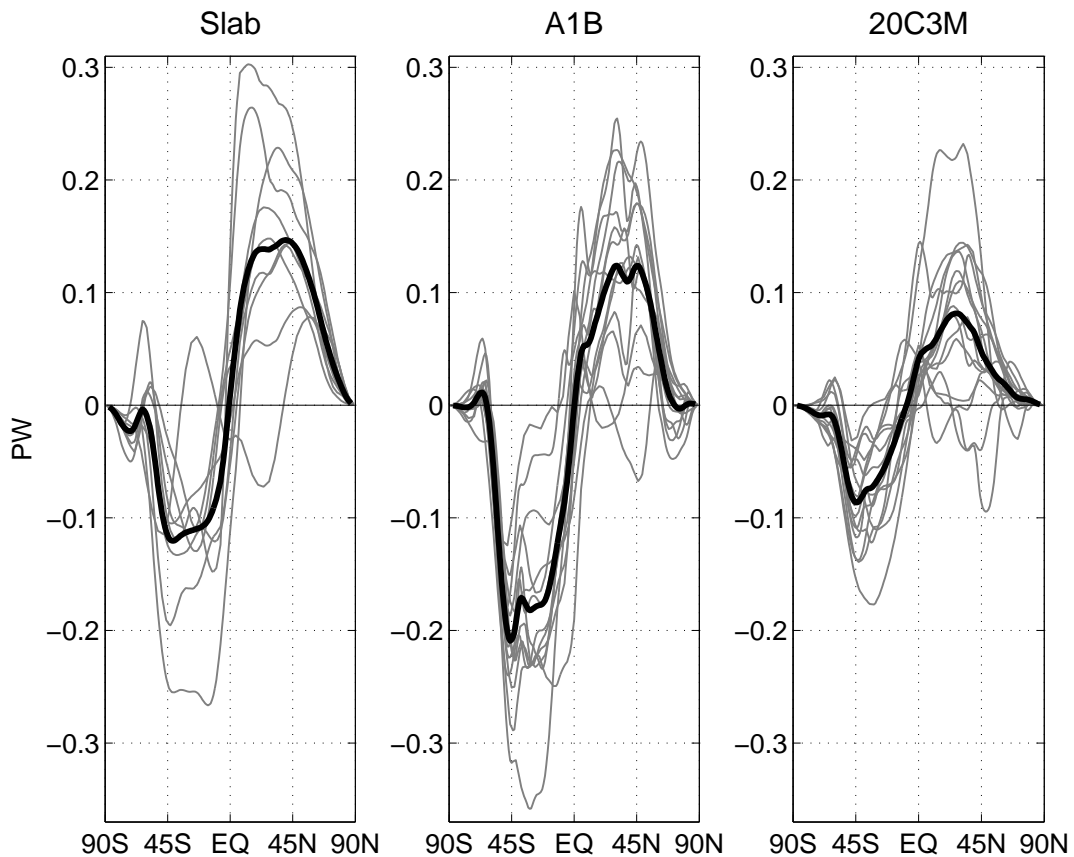

Figure 1. Zonal average changes in northward MSE flux (PW) in slab ocean models (left), the SRES A1B scenario (middle), and the 20C3M scenario (right). Multi-model means are in bold.
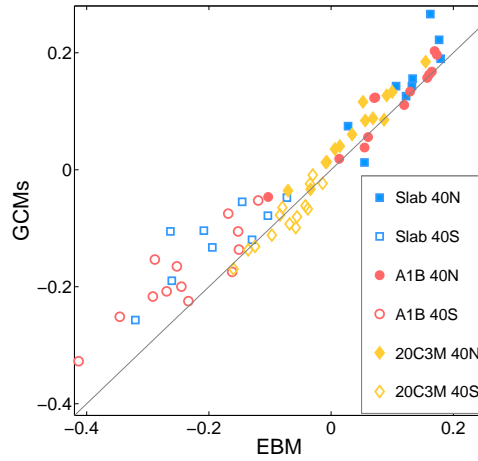
Figure 2. EBM predicted changes in MSE fluxes at 40N/S versus the actual changes in GCMs (in PW).
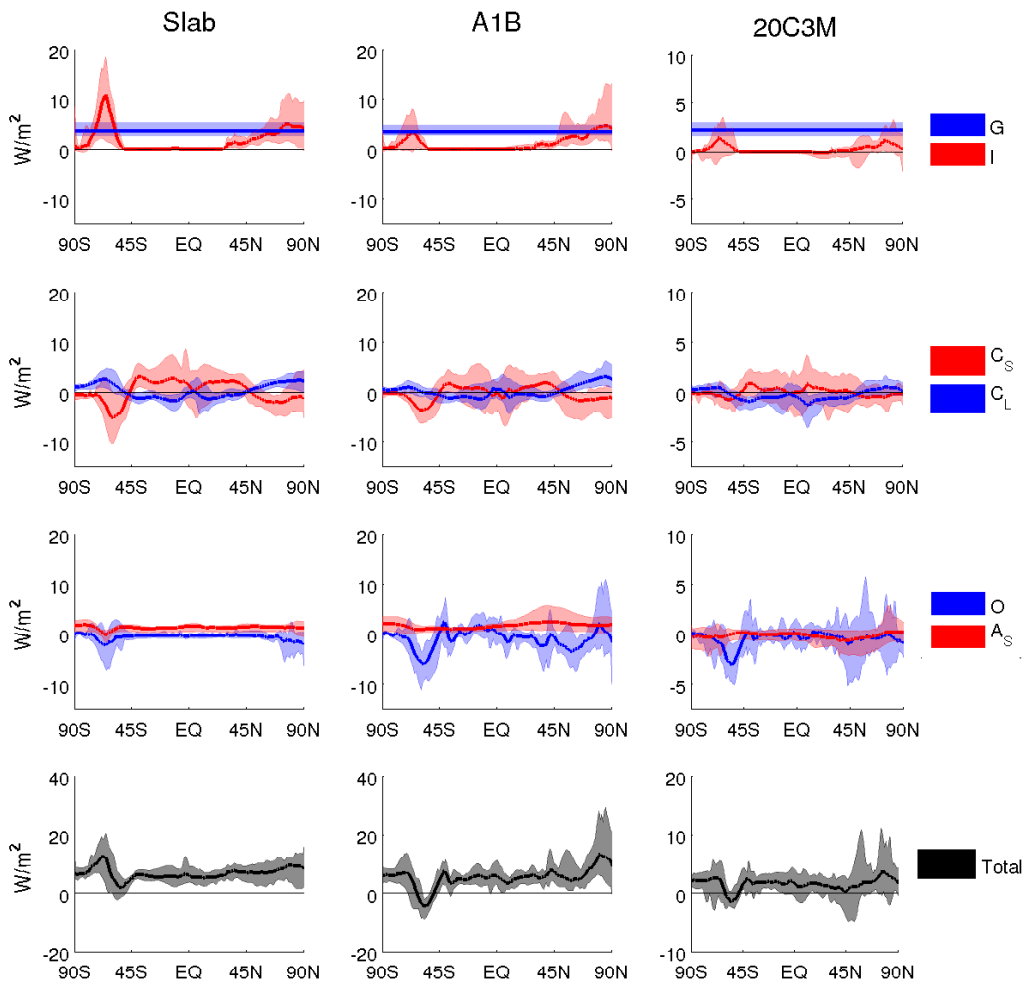

Figure 3. Changes in TOA and surface fluxes caused by individual climate components. Positive sign indicates fluxes to the atmosphere. The total is the sum of the six terms.
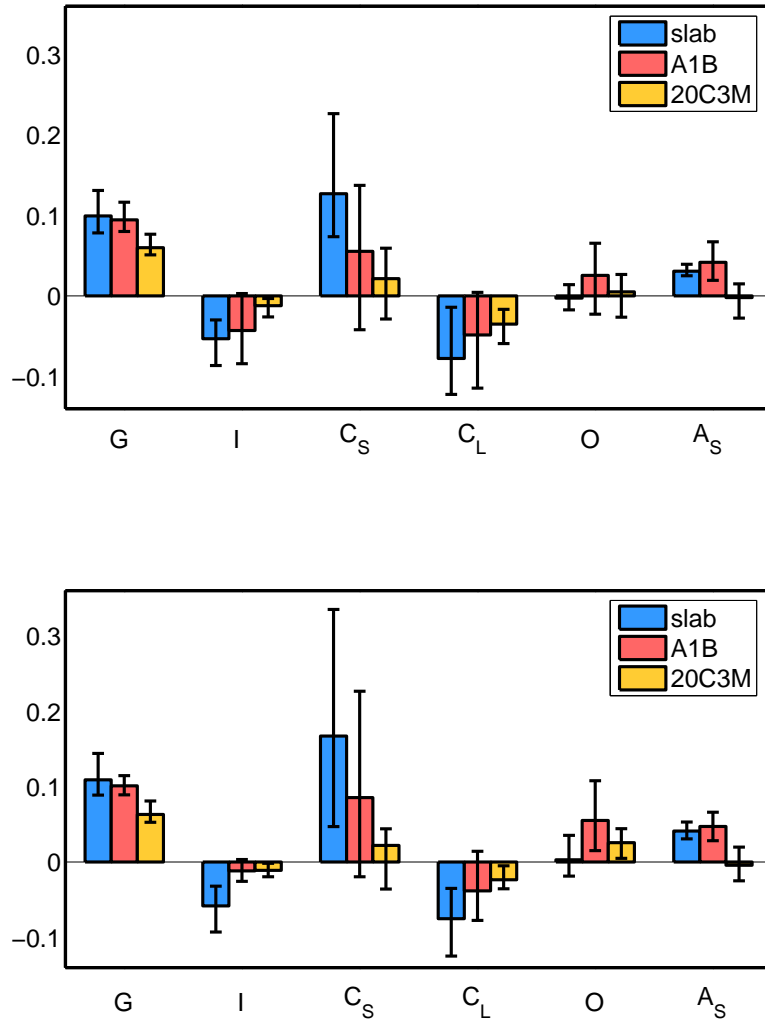
Figure 4. Attributions of changes in poleward MSE fluxes (in PW) at 40N (top) and 40S (bottom). Positive sign corresponds to increasing northward (southward) transport at 40N (40S). The bars show multi-model means of changes in poleward MSE fluxes when considering only one term at a time. The error bars indicate the second-most extreme models.